Revisiting Coulomb diamond signatures in quantum Hall interferometers

N. Moreau, S. Faniel, Fabrice Martins, L. Desplanque, X. Wallart, S. Melinte, V. Bayot, B. Hackens

Revisiting Coulomb diamond signatures in quantum Hall interferometers

N. Moreau [1,*] S. Faniel,[2,*] F. Martins [1,†] L. Desplanque [3] X. Wallart,[3] S. Melinte [2]
V. Bayot,[1] and B. Hackens [1,‡]

[1]*IMCN/NAPS, Université Catholique de Louvain, B-1348 Louvain-la-Neuve, Belgium*
[2]*ICTEAM, Université Catholique de Louvain, B-1348 Louvain-la-Neuve, Belgium*
[3]*University Lille, CNRS, Centrale Lille, JUNIA ISEN, University Polytechnique Hauts de France, UMR 8520-IEMN F-59000 Lille, France*

(Received 18 October 2021; revised 28 February 2022; accepted 15 March 2022; published 31 March 2022)

Coulomb diamonds are the archetypal signatures of Coulomb blockade, a well-known charging effect mainly observed in nanometer-sized electronic islands tunnel-coupled with charge reservoirs. Here, we identify apparent Coulomb diamond features in the scanning gate spectroscopy of a quantum point contact carved out of a semiconductor heterostructure in the quantum Hall regime. Varying the scanning gate parameters and the magnetic field, the diamonds are found to smoothly evolve to checkerboard patterns. To explain this surprising behavior, we put forward a model which relies on the presence of a nanometer-sized Fabry-Pérot quantum Hall interferometer at the center of the constriction with tunable tunneling paths coupling the central part of the interferometer to the quantum Hall channels running along the device edges. Both types of signatures, diamonds and checkerboards, and the observed transition, are reproduced by simply varying the interferometer size and the transmission probabilities at the tunneling paths. The proposed interpretation of diamond phenomenology will likely lead to revisiting previous data, and opens the way toward engineering more complex interferometric devices with nanoscale dimensions.

DOI: 10.1103/PhysRevB.105.115144

I. INTRODUCTION

When a two-dimensional electronic gas (2DEG) is placed in a large perpendicular magnetic field, charge carriers flow in one-dimensional quantum Hall edge channels (QHECs) formed as the Landau levels (LLs) cross the Fermi energy along device edges. If charge carrier phase coherence is preserved over sufficiently long distances, these edge channels can play the role of monochromatic wave beams to form quantum Hall interferometers (QHIs), the counterparts of optical interferometers in electronic systems. QHI device design relies on beamsplitters bringing the interfering QHECs in close proximity to modulate the reflection r and the transmission $t = 1 - r$ of charge carriers in and out the interferometer [1]. In this framework, Fabry-Perot (FP) [2] and Mach-Zehnder [3] QHIs have been successfully implemented, displaying clear interference due to the Aharonov-Bohm (AB) effect. They offer a promising path toward quantum computing based on anyonic braiding [4–6] as well as opportunities to test the groundwork of quantum physics, e.g., through tests of Bell inequalities violation in a Hanbury Brown and Twiss configuration [7]. Note that the latter objective can only be reached provided that QHIs have a small size compared with the phase coherence length [8].

Nevertheless, small QHIs are plagued by Coulomb charging effects, which mask AB interferences. Indeed, Coulomb blockade may also lead to oscillations of the QHI conductance when varying the magnetic flux [9,10]. Inferring the precise origin of such oscillations, and hence the regime of the studied QHI, is achieved via spectroscopy measurements. They consist of measuring the conductance through the QHI while varying both the dc bias and the magnetic flux. If the resulting map draws a checkerboard pattern, it indicates that the QHI operates in the AB regime [11–15] whereas a diamond pattern is associated to the Coulomb dominated (CD) regime in the literature [13,16,17].

Such spectroscopies, combined with scanning gate microscopy (SGM), have revealed that a QHI can form spontaneously in the vicinity of a quantum point contact (QPC) where an antidot, associated to potential inhomogeneities, couples to the counterpropagating QHECs flowing along both sides of the constriction [14,17]. Intriguingly, these QHIs have been found to exhibit both AB [14] and CD signatures [17].

Here we study a semiconductor-based 2DEG patterned in a QPC geometry in the quantum Hall (QH) regime. Thanks to SGM, we reveal the presence of a natural nanometer-sized QHI, associated with an impurity-induced quantum dot located in the vicinity of the constriction. Spectroscopy on this QHI exhibits a continuous evolution from checkerboard to diamond patterns when varying the magnetic flux. With the help of a basic FP model, we show that the transition between both types of signatures can be explained *without* invoking Coulomb charging effects. Instead, it can be reproduced, assuming a smooth change of the reflection and transmission amplitudes (r, t).

*These authors contributed equally to this paper.
†Present address: Hitachi Cambridge Laboratory, J.J. Thomson Avenue, Cambridge CB3 0HE, United Kingdom.
‡Corresponding author: benoit.hackens@uclouvain.be

II. RESULTS

A. Experimental setup

The device is built from an $In_{0.7}Ga_{0.3}As/In_{0.52}Al_{0.48}As$ quantum well grown by molecular beam epitaxy on an InP substrate (see Refs. [18,19]). A 15-nm-thick quantum well buried 25 nm below the surface hosts a 2DEG with a bare electronic density $N_S = 5.7 \times 10^{15}$ m^{-2} and a mobility $\mu = 5.3 \times 10^4$ cm^2/Vs. The 2DEG was electrically contacted by means of Ge/Au ohmic contacts. The Hall bar and the QPC were patterned using electron beam lithography and wet etching. The QPC materializes thanks to two narrow trenches defining a ∼350-nm-wide constriction [see Fig. 1(a)]. The 2DEG areas beyond the etched trenches of the QPC were used as side gates (with an applied bias V_g) to control the effective width of the constriction.

Transport measurements were performed in a dilution refrigerator (base temperature $T \approx 100$ mK) with a magnetic field B applied perpendicular to the plane of the 2DEG. The sample's resistance $R_{xx} = dV/dI$ was measured using standard ac lock-in techniques with a 2 nA excitation current and frequencies between 8 Hz and 90 Hz. The dilution refrigerator is also equipped with an atomic force microscope whose metallic tip was used as a local gate. Using this microscope, we acquired SGM images of the device by recording its resistance while the tip biased at a voltage $V_{\rm tip}$ was scanning the sample's surface at a distance of ∼60 nm. In addition, two types of spectroscopies were obtained. For this purpose, a dc electric current I_{sd} was added to the lock-in signal, and the QPC's differential resistance $R_{xx} = dV/dI|_{I_{sd}}$ was recorded as a function of I_{sd} and B or I_{sd} and $V_{\rm tip}$, keeping the tip at a fixed position.

B. Evolution of the magnetoresistance

Figure 1(b) compares the evolution of R_{xx} as a function of B with $V_g = 5$ V in two different regions of the sample: a macroscopic Hall bar (top panel) and the QPC region (bottom panel). Both curves show Shubnikov-de Haas oscillations and QH effect stemming from the magnetic depopulation of the LLs in the 2DEG. The bulk integer filling factor ν is deduced from the oscillations in the Hall bar. In the QPC trace, the more complex series of oscillations in the vicinity of the integer filling factor ν is highlighted in Fig. 1(d). Similar resistance oscillations have been reported in QPCs and were attributed to the interaction between the counterpropagating QHECs through a small QHI [see Fig. 1(c)] located in the vicinity of the constriction [14,20–25]. The same mechanisms are at play in the present sample. We will indeed show below that successive types of QHIs, whose configurations depend on the magnetic field, are located in the constriction region.

We first focus on the R_{xx} evolution around $\nu = 4$ [Fig. 1(d)] and discover four different QHI configurations as B is raised [Figs. 1(e)–1(h)]. The whole picture, detailed hereafter, relies on a peculiar electrostatic potential landscape in the constriction region, with a central dot (larger electron density) surrounded by a region of lower electron density, fully determined by disorder-related potential fluctuations. This model is further justified in Appendix A, in particular, with respect to another hypothesis involving a central antidot instead of a dot.

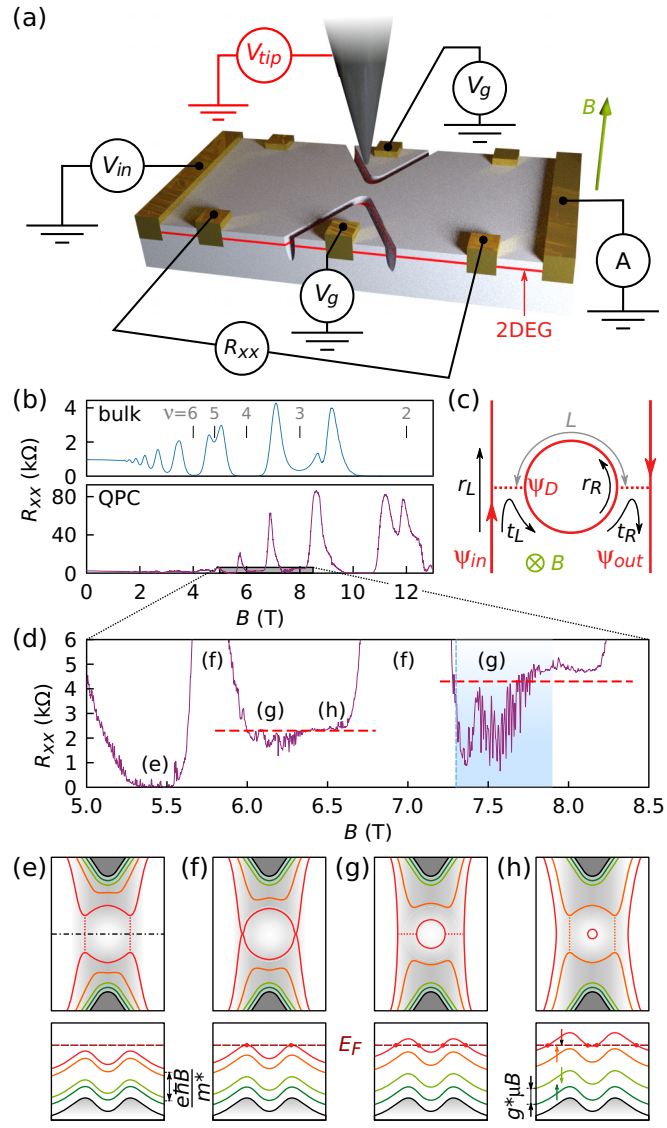

FIG. 1. (a) Artist view of the experimental setup with the buried 2DEG depicted in red. The biased tip locally changes the electron density when applying the voltage $V_{\rm tip}$ and is moved at a distance $d_{\rm tip} \sim 60$ nm above the 2DEG. A magnetic field B is applied perpendicularly to the 2DEG plane. (b) R_{xx} as a function of B measured on a Hall bar patterned next to the QPC (top panel) and in the QPC (bottom panel) with $V_g = 5$ V. The vertical lines indicate integer filling factors. (c) Schematic of a QHI formed by a QHEC loop coupling two counterpropagating QHECs (the dotted lines correspond to tunneling paths). (d) Zoom of the gray shaded region in (b). 2.2 kΩ and 4.3 kΩ plateaus are indicated with red dashed lines. (e)–(h) Evolution of the QHEC spatial configuration with B in the vicinity of the constriction (top panels) and the corresponding Landau level positions compared to the Fermi energy E_F. Higher potential (lower electron density) is depicted with darker gray shades.

At the onset of the $\nu = 4$ QH state ($5.2\,{\rm T} \lesssim B \lesssim 5.6\,{\rm T}$), R_{xx} shows a series of narrow peaks superimposed on a 0 Ω plateau. This indicates the presence of a QHI formed as the counterpropagating QHECs [red channels at the top and bottom of Fig. 1(e)] are coupled at both sides of the QPC [red dotted lines in Fig. 1(e)].

A large R_{xx} peak is then observed ($5.6\,\mathrm{T} \lesssim B \lesssim 6\,\mathrm{T}$). It is the signature of a large transmission probability between the counterpropagating QHECs, as sketched in Fig. 1(f).

As B is further increased ($6\,\mathrm{T} \lesssim B \lesssim 6.4\,\mathrm{T}$), R_{xx} exhibits dips below a $\sim 2.2\,\mathrm{k\Omega}$ plateau [red dashed line in Fig. 1(d)]. Such a plateau appears when the inner QHEC is completely backscattered so the region outside of the QPC exhibits a different filling factor (ν in the bulk) from the QPC region (filling factor ν^*), as illustrated in Fig. 1(g). In such a configuration, the resistance is given by [26]

$$R_{xx} = \frac{h}{e^2}\left(\frac{1}{\nu^*} - \frac{1}{\nu}\right), \tag{1}$$

where e is the electron charge and h is the Planck's constant. The $2.2\,\mathrm{k\Omega}$ plateau is consistent with $\nu = 4$ and $\nu^* = 3$. It indicates that the spin degeneracy of the LLs has been lifted due to Zeeman effect [27]. The second LL (and its corresponding QHEC) is therefore split in two states: one spin-down polarized [in red in Figs. 1(e)–1(h)] and one spin-up polarized (in orange). Based on this picture, the dips below the plateau are explained by the presence of a dot (QHEC loop) at the center of the constriction which acts as a QHI coupling the QHECs running at the left and right sides of the QPC in Fig. 1(g). When the QHI formed by this dot [Fig. 1(c)] is active, these QHECs are not perfectly backscattered anymore and R_{xx} drops below the $2.2\,\mathrm{k\Omega}$ plateau.

In the next B range ($6.4\,\mathrm{T} \lesssim B \lesssim 6.7\,\mathrm{T}$), R_{xx} peaks are observed above the $2.2\,\mathrm{k\Omega}$ plateau. This magnetoresistance sequence is close to the first regime [Fig. 1(e)] but the QHI is created by the spin up-polarized QHEC while the spin down-polarized QHEC is perfectly backscattered [Fig. 1(h)].

When B is further increased, the regimes highlighted in Fig. 1(d) are repeated with the spin up-polarized QHEC. R_{xx} then features fluctuations around a plateau close to $4.3\,\mathrm{k\Omega}$ [right red dashed line in Fig. 1(d)], corresponding to the filling factors $\nu = 3$ and $\nu^* = 2$ in Eq. (1). In the remainder of this paper, we will further characterize the QHI formed by the spin-up polarized QHEC in the configuration of Fig. 1(g).

C. dc bias spectroscopies

Figure 2(a) displays a R_{xx} map as a function of the electrically biased tip position, with the etched area defining the constriction indicated by the white shaded regions. This map features concentric fringes centered on the QPC, which clearly confirms that the QHI is located in the constriction. In the AB framework, these oscillations originate from a change of the magnetic flux $\Phi = BA$ enclosed in the QHI whose area A varies when the electrically biased tip moves in its vicinity. As a result, interference conditions in the QHI alternate between constructive and destructive, which yields concentric fringes in the SGM image. Note that another explanation could be given for the same phenomenon in the framework of the CD regime (with the tip influencing energy levels of a tunnel-coupled quantum dot), but we will see below that we can discard this hypothesis.

Figure 2(b) shows R_{xx} as a function of V_{tip} for the tip position indicated with a green dot in Fig. 2(a). When V_{tip} is tuned to large negative values (below $\sim -3\,\mathrm{V}$), R_{xx} reaches the $4.3\,\mathrm{k\Omega}$ plateau, decorated with a set of narrow dips. This

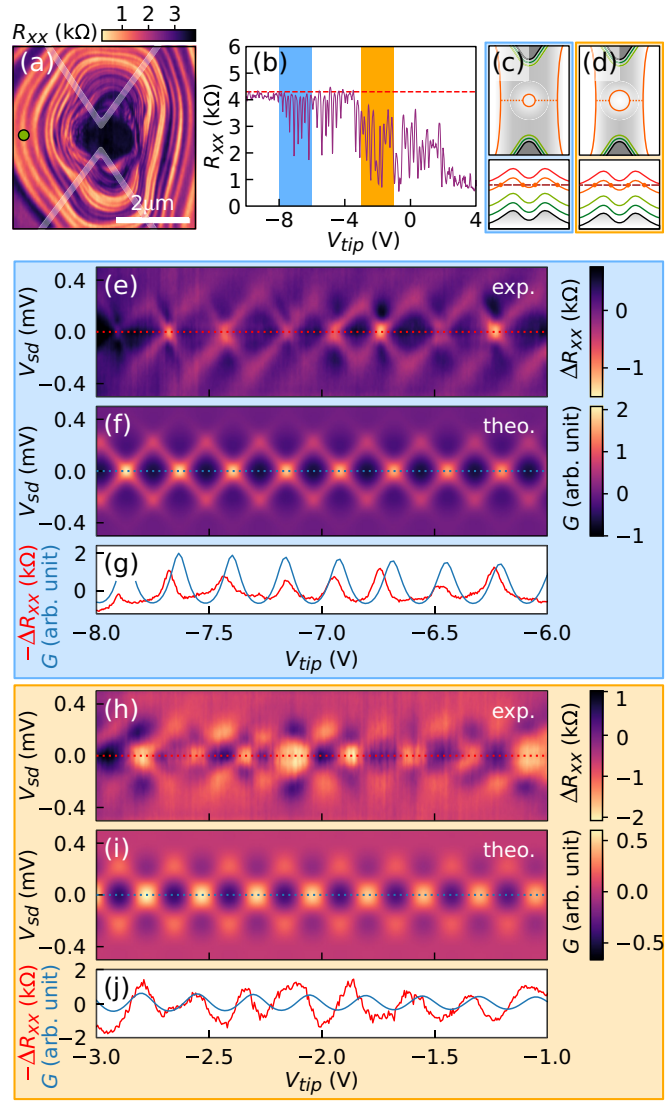

FIG. 2. (a) SGM map obtained by recording R_{xx} as a function of the tip position at $B = 7.3$ T [blue dashed line in Fig. 1(d)] and with $V_{\mathrm{tip}} = 0\,\mathrm{V}$ (depleting tip due to the work function difference with the sample surface). The QPC borders are indicated by the white shaded area. (b) Evolution of R_{xx} with V_{tip} for the tip position indicated with a green dot in (a). The red dashed lines indicates the $4.3\,\mathrm{k\Omega}$ plateau. (c), (d) Evolution of the QHECs spatial configuration with V_{tip} in the vicinity of the constriction (top panels) and the corresponding Landau level positions compared to the Fermi energy E_F (bottom panel). (c) and (d) correspond, respectively, to the blue and orange regions in (b). (e), (f) Experimental map of ΔR_{xx} and simulated map of G, respectively, as a function of V_{sd} and V_{tip} [blue region in (b)]. The maps feature diamond patterns. (g) ΔR_{xx} at $V_{sd} = 0$ from (e) in red and G versus V_{tip} from (f) in blue. (h), (i) Experimental map of ΔR_{xx} and simulated map of G, respectively, as a function of V_{sd} and V_{tip} [orange region in (b)]. The maps feature checkerboard patterns. (j) ΔR_{xx} at $V_{sd} = 0$ from (h) in red and G versus V_{tip} from (i) in blue.

behavior is perfectly consistent with the picture presented in Fig. 1. Indeed, a negative V_{tip} decreases the electron density (i.e., the electrostatic potential landscape shifts upward) which implies a smaller QHI size. Consequently, the transmission probability to the backscattered QHECs is decreased

[Fig. 2(c)] compared to a less negative V_{tip} [Fig. 2(d)]. With a smaller transmission probability, R_{xx} remains close to the plateau that corresponds to a perfect backscattering of the QHECs.

Next, we compare the dc bias spectroscopies in the blue (weak transmission) and orange (stronger transmission) ranges in Fig. 2(b) to obtain further information on the different regimes of transmission between the dot and the QHECs. In such measurements, one records R_{xx} as a function of V_{tip} and the source-drain voltage V_{sd}. Both parameters change the phase of the QHI. A high-pass filter has been applied to each map to get rid of the broad background evolution of R_{xx} and only keep the oscillations ΔR_{xx} originating from the QHI. First, Fig. 2(e) shows the spectroscopy obtained at large negative values of V_{tip} [weak transmission - blue in Fig. 2(b)]. In this situation, ΔR_{xx} features a characteristic diamond pattern, usually associated with Coulomb charging effects [13,16,17]. Second, when examining data at less negative values of V_{tip} [stronger transmission—orange in Fig. 2(b)], the obtained spectroscopy displays a checkerboard pattern [Fig. 2(h)]. The latter pattern is the signature observed in QHIs in the AB regime [11–15,28–31].

However, the apparent transition from the AB to CD regime when varying V_{tip} seems surprising for at least two reasons. First, the characteristic energy scales in V_{sd} are expected to be different, because they are ascribed to different and uncorrelated mechanisms: a phase change explains the AB oscillations in V_{sd} whereas the Coulomb charging energy should determine the height of the Coulomb diamonds. Interestingly, the energy scale extracted from the spectroscopies in Figs. 2(e) and 2(h) remains the same for the checkerboard and the diamonds, with a value around 0.2 mV. Second, the Coulomb charging energy is determined by the size of the QHI and we will show in the next section that this size does not change significantly within the V_{tip} range of Fig. 2. Therefore, if the Coulomb charging energy does not dominate in Fig. 2(h), nor should it in Fig. 2(e). Figures 3(c) and 3(d), obtained by varying B instead of V_{tip}, confirms that the checkerboard pattern [Fig. 3(c)] evolves continuously, and with a constant energy scale in V_{sd}, to a diamond pattern [Fig. 3(d)] with a small increase of the magnetic flux enclosed in the QHI.

Studying the evolution of R_{xx} oscillation amplitude ΔR_{xx} with the temperature yields a third reason to discard the hypothesis of a different origin for checkerboard and diamond patterns. The oscillation amplitude associated with both patterns [orange and blue regions in Fig. 3(a)] turns out to follow the same exponential dependence $\Delta R_{xx} = \Delta R_{xx,0} \exp(-T/T_0)$ with the temperature T [Fig. 3(b)], consistent with the AB effect [14]. The CD regime, on the contrary, would imply a T^{-1} dependence [25]. These observations suggest that the QHI remains in the pure AB regime, whatever the observed phenomenology (checkerboard- or diamondlike). In that framework, it remains to explain how a diamond pattern can be observed in the AB regime.

III. DISCUSSION

To explain the transition between checkerboard and diamond patterns in Figs. 2(e), 2(h), 3(c), and 3(d), we

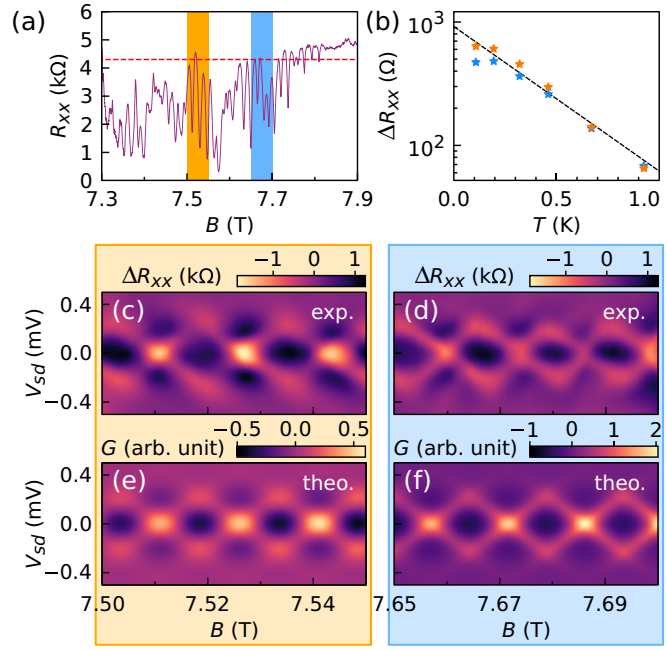

FIG. 3. (a) R_{xx} versus B [blue region in Fig. 1(d)] with $V_{tip} = 0$ V. The red dashed line indicates the 4.3 kΩ plateau. (b) Oscillation amplitude ΔR_{xx} measured at different temperatures T for the two ranges of B [orange and blue regions in (a)]. The temperature dependence, fitted with a continuous line, displays a similar exponential evolution for both B ranges. (c), (d) Experimental map of ΔR_{xx} and simulated map of G as a function of V_{sd} and B. (e), (g) Zooms on the low B range of (c), (d) displaying a checkerboard pattern. (f), (h) Zooms on the high B range of (c), (d) displaying a diamond pattern.

have considered that the QHI always acts as a simple FP interfometer in the AB regime whatever the V_{tip} or B range. From this hypothesis, we have developed a model inspired from Ref. [30] and described in details in Appendix B. Our model relies on the schematic shown in Fig. 1(c), where the FP QHI is formed by a closed-loop QHEC (inside a dot) connected to the left (input) and the right (output) QHECs by two beam splitters (dotted lines).

Hereafter, we show that this model accurately reproduces the experimental spectroscopy results. Before developing the comparison between experimental and simulation results, we should stress that experiment yields maps of ΔR_{xx}, the oscillating component of the resistance through the sample, whereas model results, obtained from Eq. (B7), correspond to oscillating components of the conductance G through the dot. The two quantities are directly linked since a large value of G favors the transport through the QPC, lowering R_{xx} below the plateau value, and therefore increasing ΔR_{xx}. Note also that the spectroscopies shown in Figs. 2(e), 2(h), 3(c), and 3(d) feature a decrease of the oscillations visibility when $|V_{sd}|$ is raised. Nevertheless, the origin of the phase randomization mechanism leading to this behavior is debated in the literature and a consensual explanation is still missing [32–35]. Here, we have modeled the visibility decay with a Gaussian function [Eq. (B7)] fitted to the data.

The correspondence between the simulated G and experimental ΔR_{xx} spectroscopies is illustrated in

Figs. 2(e), 2(f), 2(h), and 2(i). Both simulated maps were obtained with the same parameters in Eq. (B7): $B = 7.3$ T as in the experiment, the QHEC velocity $v = 0.5 \times 10^5$ m/s and the parameters associated to the visibility decay $\gamma = 1$ and $\Delta V_{sd} = 0.6$ mV. The following parameters were the only ones adjusted when changing V_{tip}: $L = 404.6$ nm and $R_L = R_R = 0.05$ at $V_{\text{tip}} = -8$ V, and $L = 435.1$ nm and $R_L = R_R = 0.3$ at $V_{\text{tip}} = -1$ V. (These values were used to find the free parameters in Eqs. (B8) and (B9)]. Three main outcomes can be highlighted from simulation results, and the good fit to the experimental data: (i) At large negative V_{tip}, a good correspondence has been obtained for a small dot size and a large reflection probability (weak transmission) and a diamond pattern is observed in this case, whereas at smaller negative V_{tip} (larger dot, stronger transmission), the model yields a checkerboard pattern. (ii) The dot size obtained from a fit to the AB oscillation is fully consistent with the constriction width of 350 nm. Indeed, the dot diameter is around 250 nm. (iii) The QHEC velocity v used to fit the V_{sd} oscillations is fully consistent with values obtained in previous studies [13,14].

Figures 3(e) and 3(f) also show that the model can accurately reproduce the experimental data of Figs. 3(c) and 3(d), respectively. The simulations have been performed with an evolution of the QHI parameters from $L = 427.3$ nm and $R_L = R_R = 0.3$ at $B = 7.5$ T to $L = 407.8$ nm and $R_L = R_R = 0.05$ at $B = 7.7$ T. The other constant parameters are the same as in Fig. 2. Again, the dot shape evolution and its coupling to QHECs follow the pictures proposed in Fig. 1(g), with a size and a transmission probability decreasing with the magnetic field. This set of maps further draws a clear overview of the evolution from a checkerboard to a diamond pattern as the dot geometry and transmission are changed.

At this point, it is worth providing an intuitive physical picture explaining how diamond patterns, very similar to Coulomb blockade signatures, can emerge in FP QHIs. Figures 2(g) and 2(j) show the measured R_{xx} and the simulated G as a function of V_{tip} at zero V_{sd}. The curves extracted from the diamond pattern [Fig. 2(g)] exhibit sharp peaks whereas the ones corresponding to the checkerboard pattern [Fig. 2(j)] are characterized by a smooth sinusoidal evolution. This is consistent with the FP theory where resonances narrow as the reflection is increased at the interferometer beam splitters, due to recursive interference of the electronic waves partially confined in the interferometer: the sharpness of the QHI resonances is related to the quality factor or the finesse of the cavity. When applying a V_{sd} bias, an extra phase is accumulated by the charge carriers [Eq. (B4) in Appendix B], leading to a shift of the sharp resonances for large reflection probabilities at the beam splitters and, hence, to the characteristic diamond features of Figs. 2(e) and 2(f). With smaller reflection probabilities, the bias-induced phase shift is initially less visible than in the former case as resonances are broader and is also masked by the bias-induced loss of visibility. The dephasing then appears more abruptly at larger V_{sd}, resulting in the checkerboard pattern of Figs. 2(h) and 2(i).

Note also that similar observations (diamond patterns) were already reported in the case of FP cavities formed in carbon nanotubes between partially transmitting metallic contacts [36]. In the latter case, sets of parallel lines were observed, reminiscent of excited states signatures in Coulomb diamonds, but captured by a FP model. Our data also show faint signatures of parallel lines in some cases, e.g., around $V_{\text{tip}} = -7.1$ V in Fig. 2(e). The latter lines could, however, be related to a mixture of different effects such as the activation of different QHIs in parallel (whose signatures would then superimpose) or of additional tunneling channel within the same QHI. The SGM map in Fig. 2(a), obtained at $V_{\text{tip}} = 0$ V also points toward more complex behavior when the tip approaches the constriction region (multiple crossings between resonance lines) or, at a fixed tip position, when V_{tip} becomes more negative [equivalent to expanding the SGM pattern in Fig. 2(a)]. Further data would be necessary to disentangle this type of complex phenomena but this is beyond the scope of this paper.

As discussed above, we have accurately reproduced the experimental spectroscopy data in Figs. 2 and 3 with a model of QHI operating in the AB regime and whose radius is around 125 nm ($A < 0.05\,\mu\text{m}^2$). We have also observed QHIs functioning in the same regime with similar sizes in graphene [37]. However, up to our knowledge, no QHI operating in the AB has ever been reported with a size under 1 μm^2, even with architectures optimized to reduce Coulomb interactions [15,30,31]. According to Ref. [1], finding a QHI in the AB or CD regime depends on the capacitive coupling between the QHEC loop forming the QHI and the localized states enclosed in the QHI, caused by potential fluctuations. When the QHI size decreases, the capacitive coupling is enhanced and Coulomb interactions tend to dominate the transport. The main difference between the configuration measured here and previous studies is the absence of localized states inside the QHEC loop forming the QHI: the quantum dot confinement results from a simple single dip in the potential landscape [Fig. 1(g)]. This advantageous potential landscape is the key to reach a fully AB-dominated regime in nanoscale QHI.

A last point to discuss is the generality of the results exposed in this paper. Indeed, the transitions between the different regimes of Fig. 1(d), due to a FP interferometer coupling the counterpropagating QHECs, requires the presence of a dot located in the vicinity of the constriction. Whereas this configuration seems specific to the studied sample, dots or antidots coupling counterpropagating QHECs have been highlighted thanks to SGM in several other samples, being in the vicinity constrictions in semiconductor-based 2DEGs [14,17,25] or along the edges in graphene devices [38]. Therefore, this shows that random potential fluctuations, ubiquitous even in relatively high mobility two-dimensional electron systems, indeed provide various natural pinning locations for dots and antidots mediating coupling between counterpropagating QHECs. Based on this paper, one can then devise more elaborated architectures, where the position and potential landscape giving rise to the dots or antidots could be predetermined and tuned by a local gate.

IV. CONCLUSION

In this paper, we have used SGM to reveal the presence of a quantum dot located in the vicinity of a QPC. In the QH regime, it acts as a FP inteferometer that modulates electrons backscattering between the two sides of the QPC.

dc bias-spectroscopies reveal a continuous transition from checkerboard to diamonds patterns. With a simple FP model, we have shown that both patterns can be explained in a fully AB (coherent) regime: this represents a paradigm shift in the field, compared to the usual practice that automatically associates diamond patterns in the spectroscopy with the CD regime. We associate the observed transition with a change of transmission probability between the central QHEC loop and the counterpropagating QHECs flowing at each side of the QPC. Finally, we point out that finding a QHI with a size of a few hundreds of nanometers in a pure AB regime is surprising since it should yield a large charging energy. We resolve this apparent contradiction by pointing that no localized state exists inside the QHI, lowering strongly the probability of emergence of Coulomb interactions, a behavior also observed in graphene [37]. Our paper therefore paves the way toward the design of nano-sized QHIs, allowing us to feature both a pure AB regime and a coherence length much larger than the interferometer size, two key ingredients in the progress toward anyonic braiding and tests of quantum physics groundwork.

ACKNOWLEDGMENTS

This work has been supported by FRFC Grants No. 2.4.546.08.F and No. 2.4503.12, FNRS Grant No. 1.5.044.07.F, by the FSR and ARC programs Stresstronics and NATURIST, by BELSPO (Interuniversity Attraction Pole IAP-6/42), and by the PNANO 2007 program of the ANR (MICATEC project). B.H. (research associate) and N.M. (FRIA fellowship) acknowledge financial support from the Fonds De La Recherche Scientifique - FNRS of Belgium.

APPENDIX A: DOT OR ANTIDOT?

In Figs. 1(e)–1(h), we have presented the QHEC configurations in the vicinity of the QPC that explains the transport curve of Figs. 1(b) and 1(d). This relies on a global decrease of the electron density in the constriction region and a local increase of the density, due to potential inhomogeneities, forming a quantum dot in the center of the constriction. However, similar transport data in the literature have been explained with the presence of an antidot near the QPC, associated with a local decrease of the electron density [14,20,23–25]. In this Appendix, we justify why the latter model (antidot), despite being simpler, is not consistent with the present data.

Figure 4 presents the QHEC configurations in the situation where an antidot is located in the center of the constriction. At first sight, the four configurations are compatible with the different regimes in Fig. 1(d). However, Fig. 4(c) presents a first inconsistency. Indeed, we have shown that the spin degeneracy is lifted and the third (orange) and fourth (red) LLs are polarized with opposite spins. Therefore, the tunneling between the counterpropagating QHECs via the antidot in Fig. 4(c) is prohibited.

A second argument against the antidot model [and hence in favor of the model proposed in Figs. 1(e)–1(h)] is found in the R_{xx} evolution versus V_{tip} in Fig. 2(b). As discussed in the main text, large negative values of V_{tip}, leading to a decrease of the electron density, are associated with high reflection

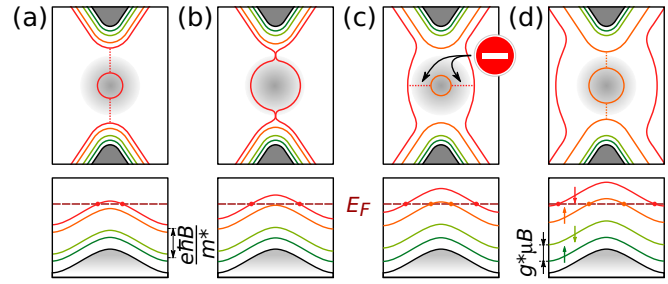

FIG. 4. (a)–(d) Evolution of the QHEC spatial configuration with B in the vicinity of an antidot located in the center of the constriction (top panels) and the corresponding Landau-level position compared to the Fermi energy E_F. A high potential (low electron density) is depicted with darker gray shades.

probabilities at the QHI beam splitters. It is inconsistent with the antidot model where a decrease of the electron density should yield a larger antidot, closer to the counterpropagating QHECs, leading to a smaller reflection coefficient at the beam splitters (due to a higher transmission probability between the QHECs and the antidot). On the contrary, the model of Figs. 1(e)–1(h) correctly captures the evolution of the transmission probability with V_{tip}.

APPENDIX B: FABRY-PEROT MODEL

In this Appendix, we develop the model used to produce the simulated maps of Figs. 2 and 3. It relies on the schematic shown in Fig. 1(c). In that framework, the wave function ψ_D at the left side of the dot can be written

$$\psi_D = it_L\psi_{\text{in}} + r_R r_L \exp(i2\phi_D)\psi_D, \tag{B1}$$

where t_L is the transmission amplitude at the left side of the dot, r_L and r_R are the reflection amplitude at the left and right sides of the dot, ψ_{in} is the wave function of the left QHEC and ϕ_D is the phase accumulated along one arm of the QHI with a length $L = \sqrt{\pi A}$. Following the same logic, the wave function of the right QHEC is given by

$$\psi_{\text{out}} = it_R \exp(i\phi_D)\psi_D, \tag{B2}$$

where t_R is the transmission amplitude at the right side of the dot. From Eqs. (B1) and (B2), we define the transmission probability through the dot $T = |\psi_{\text{out}}|^2/|\psi_{\text{in}}|^2$ as a function of the reflection probabilities at each beam splitter $R_{L(R)} = |r_{L(R)}|^2 = 1 - |t_{L(R)}|^2$ and we obtain

$$T(\phi_D) = \frac{(1-R_L)(1-R_R)}{1+R_L R_R - 2\sqrt{R_L R_R}\cos(\phi_D)}. \tag{B3}$$

This transmission depends on the phase ϕ_D that can be developed as [39]

$$\phi_D(\epsilon, \Phi) = \pi\frac{\Phi}{\Phi_0} + \frac{L\epsilon}{\hbar v} + \varphi, \tag{B4}$$

where the first term of the sum is the AB phase, with $\Phi_0 = h/2e$ the quantum of magnetic flux, the second term is the phase associated with the source-drain bias-induced energy shift ϵ, where v is the QHEC velocity in the QHI and the third term φ is a constant phase. From Eq. (B3), one can extract the

oscillating component of the transmission by subtracting the average term $\langle T(\epsilon, \Phi)\rangle$. It yields

$$T_{\rm osc}(\epsilon, \Phi) = T(\epsilon, \Phi) - \frac{(1-R_L)(1-R_R)}{1+R_L R_R}. \tag{B5}$$

The oscillation component of the current through the dot can then be expressed as

$$I_{\rm osc} = \frac{-e}{h}\int_{-eV_{sd}/2}^{eV_{sd}/2} T_{\rm osc}(\epsilon, \Phi)d\epsilon, \tag{B6}$$

where V_{sd} is the dc source-drain bias voltage. We assume an equal voltage drop at both beam splitters. The conductance G through the QHI is obtained from Eq. (B6) and the visibility decay is modeled with a Gaussian function in V_{sd} as [12–14]

$$G = \frac{dI_{\rm osc}}{dV_{sd}} \exp\left(-2\pi\gamma\left(\frac{V_{sd}}{\Delta V_{sd}}\right)^2\right), \tag{B7}$$

where γ and ΔV_{sd} are fitting parameters.

In the experimental spectroscopies of Figs. 2 and 3, the AB phase evolves with Φ [Eq. (B4)] through $V_{\rm tip}$ or B. Indeed, both parameters tune the dot area A as illustrated in Figs. 1(f)–1(h) for a change of B, modifying the spacing between the LLs, and in Figs. 2(e) and 2(h) for a change of $V_{\rm tip}$, shifting the potential and the LLs compared to the Fermi energy E_F. The QHI size, given by the arm length L, then evolves as

$$dL = \frac{\partial L}{\partial V_{\rm tip}} dV_{\rm tip} + \frac{\partial L}{\partial B} dB. \tag{B8}$$

Since the terms $\partial L/\partial V_{\rm tip}$ and $\partial L/\partial B$ are extremely difficult to assess, we assume that they are constant. The evolution of L with $V_{\rm tip}$ and B is therefore linear.

Furthermore, any change of the dot size also affects its proximity, and hence its transmission probability [dotted lines in Figs. 1(e)–1(h) and Figs. 2(e)–2(h)], with the backscattered QHECs. Since the coupling occurs through tunneling, the associated transmission probability evolves exponentially with the distance between the dot and the QHECs. In turn, since this distance evolves linearly with the dot size, one has

$$R_{L(R)} = \alpha \exp(-\beta L), \tag{B9}$$

where α and β are positive coefficients to ensure that the reflection probability increases when the dot size decreases [see Fig. 1(c)]. This expression is only valid when $R_{L(R)} \ll 1$.

[1] B. I. Halperin, A. Stern, I. Neder, and B. Rosenow, Theory of the Fabry-Pérot quantum Hall interferometer, Phys. Rev. B **83**, 155440 (2011).

[2] B. J. van Wees, L. P. Kouwenhoven, C. J. P. M. Harmans, J. G. Williamson, C. E. Timmering, M. E. I. Broekaart, C. T. Foxon, and J. J. Harris, Observation of Zero-Dimensional States in a One-Dimensional Electron Interferometer, Phys. Rev. Lett. **62**, 2523 (1989).

[3] Y. Ji, Y. Chung, D. Sprinzak, M. Heiblum, D. Mahalu, and Hadas Shtrikman, An electronic Mach-Zehnder interferometer, Nature (London) **422**, 415 (2003).

[4] C. Bäuerle, D. C. Glattli, T. Meunier, F. Portier, P. Roche, P. Roulleau, S. Takada, and X. Waintal, Coherent control of single electrons: A review of current progress, Rep. Prog. Phys. **81**, 056503 (2018).

[5] J. Nakamura, S. Liang, G. C. Gardner, and M. J. Manfra, Direct observation of anyonic braiding statistics, Nat. Phys. **16**, 931 (2020).

[6] H. Bartolomei, M. Kumar, R. Bisognin, A. Marguerite, J.-M. Berroir, E. Bocquillon, B. Plaçais, A. Cavanna, Q. Dong, U. Gennser, Y. Jin, and G. Fève, Fractional statistics in anyon collisions, Science **368**, 173 (2020).

[7] P. Samuelsson, E. V. Sukhorukov, and M. Büttiker, Two-Particle Aharonov-Bohm Effect and Entanglement in the Electronic Hanbury Brown–Twiss Setup, Phys. Rev. Lett. **92**, 026805 (2004).

[8] I. Neder, N. Ofek, Y. Chung, M. Heiblum, D. Mahalu, and V. Umansky, Interference between two indistinguishable electrons from independent sources, Nature (London) **448**, 333 (2007).

[9] Y. Zhang, D. T. McClure, E. M. Levenson-Falk, C. M. Marcus, L. N. Pfeiffer, and K. W. West, Distinct signatures for Coulomb blockade and Aharonov-Bohm interference in electronic Fabry-Perot interferometers, Phys. Rev. B **79**, 241304(R) (2009).

[10] A. Kou, C. M. Marcus, L. N. Pfeiffer, and K. W. West, Coulomb Oscillations in Antidots in the Integer and Fractional Quantum Hall Regimes, Phys. Rev. Lett. **108**, 256803 (2012).

[11] I. Neder, M. Heiblum, Y. Levinson, D. Mahalu, and V. Umansky, Unexpected Behavior in a Two-Path Electron Interferometer, Phys. Rev. Lett. **96**, 016804 (2006).

[12] P. Roulleau, F. Portier, D. C. Glattli, P. Roche, A. Cavanna, G. Faini, U. Gennser, and D. Mailly, Finite bias visibility of the electronic Mach-Zehnder interferometer, Phys. Rev. B **76**, 161309(R) (2007).

[13] D. T. McClure, Y. Zhang, B. Rosenow, E. M. Levenson-Falk, C. M. Marcus, L. N. Pfeiffer, and K. W. West, Edge-State Velocity and Coherence in a Quantum Hall Fabry-Pérot Interferometer, Phys. Rev. Lett. **103**, 206806 (2009).

[14] F. Martins, S. Faniel, B. Rosenow, H. Sellier, S. Huant, M. G. Pala, L. Desplanque, X. Wallart, V. Bayot, and B. Hackens, Coherent tunnelling across a quantum point contact in the quantum Hall regime, Sci. Rep. **3**, 1416 (2013).

[15] J. Nakamura, S. Fallahi, H. Sahasrabudhe, R. Rahman, S. Liang, G. C. Gardner, and M. J. Manfra, Aharonov-Bohm interference of fractional quantum Hall edge modes, Nat. Phys. **15**, 563 (2019).

[16] M. Kataoka, C. J. B. Ford, G. Faini, D. Mailly, M. Y. Simmons, D. R. Mace, C.-T. Liang, and D. A. Ritchie, Detection of Coulomb Charging Around an Antidot in the Quantum Hall Regime, Phys. Rev. Lett. **83**, 160 (1999).

[17] F. Martins, S. Faniel, B. Rosenow, M. G. Pala, H. Sellier, S. Huant, L. Desplanque, X. Wallart, V. Bayot, and B. Hackens, Scanning gate spectroscopy of transport across a quantum Hall nano-island, New J. Phys. **15**, 013049 (2013).

[18] S. Toussaint, B. Brun, S. Faniel, L. Desplanque, X. Wallart, V. Bayot, and B. Hackens, Two-dimensional rutherford-like scattering in ballistic nanodevices, Phys. Rev. B **98**, 075310 (2018).

[19] S. Toussaint, F. Martins, S. Faniel, M. G. Pala, L. Desplanque, X. Wallart, H. Sellier, S. Huant, V. Bayot, and B. Hackens, On the origins of transport inefficiencies in mesoscopic networks, Sci. Rep. **8**, 3017 (2018).

[20] C. J. B. Ford, P. J. Simpson, I. Zailer, D. R. Mace, M. Yosefin, M. Pepper, D. A. Ritchie, J. E. F. Frost, M. P. Grimshaw, and G. A. C. Jones, Charging and double-frequency Aharonov-Bohm effects in an open system, Phys. Rev. B **49**, 17456 (1994).

[21] J. A. Simmons, S. W. Hwang, D. C. Tsui, H. P. Wei, L. W. Engel, and M. Shayegan, Resistance fluctuations in the integral- and fractional-quantum-Hall-effect regimes, Phys. Rev. B **44**, 12933 (1991).

[22] S. W. Hwang, J. A. Simmons, D. C. Tsui, and M. Shayegan, Quantum interference in two independently tunable parallel point contacts, Phys. Rev. B **44**, 13497 (1991).

[23] V. J. Goldman and B. Su, Resonant tunneling in the quantum Hall regime: Measurement of fractional charge, Science **267**, 1010 (1995).

[24] V. J. Goldman, J. Liu, and A. Zaslavsky, Electron tunneling spectroscopy of a quantum antidot in the integer quantum Hall regime, Phys. Rev. B **77**, 115328 (2008).

[25] B. Hackens, F. Martins, S. Faniel, C. A. Dutu, H. Sellier, S. Huant, M. Pala, L. Desplanque, X. Wallart, and V. Bayot, Imaging Coulomb islands in a quantum Hall interferometer, Nat. Commun. **1**, 39 (2010).

[26] M. Büttiker, Absence of backscattering in the quantum Hall effect in multiprobe conductors, Phys. Rev. B **38**, 9375 (1988).

[27] M. A. Paalanen, D. C. Tsui, and A. C. Gossard, Quantized Hall effect at low temperatures, Phys. Rev. B **25**, 5566 (1982).

[28] Di S. Wei, T. van der Sar, J. D. Sanchez-Yamagishi, K. Watanabe, T. Taniguchi, P. Jarillo-Herrero, B. I. Halperin, and A. Yacoby, Mach-Zehnder interferometry using spin- and valley-polarized quantum Hall edge states in graphene, Sci. Adv. **3**, e1700600 (2017).

[29] M. Jo, P. Brasseur, A. Assouline, G. Fleury, H.-S. Sim, K. Watanabe, T. Taniguchi, W. Dumnernpanich, P. Roche, D. C. Glattli, N. Kumada, F. D. Parmentier, and P. Roulleau, Quantum Hall Valley Splitters and a Tunable Mach-Zehnder Interferometer in Graphene, Phys. Rev. Lett. **126**, 146803 (2021).

[30] C. Déprez, L. Veyrat, H. Vignaud, G. Nayak, K. Watanabe, T. Taniguchi, F. Gay, H. Sellier, and B. Sacépé, A tunable Fabry-Pérot quantum Hall interferometer in graphene, Nat. Nanotechnol. **16**, 555 (2021).

[31] Y. Ronen, T. Werkmeister, D. Haie Najafabadi, A. T. Pierce, L. E. Anderson, Y. J. Shin, S. Y. Lee, Y. H. Lee, B. Johnson, K. Watanabe, T. Taniguchi, A. Yacoby, and P. Kim, Aharonov-Bohm effect in graphene-based Fabry-Pérot quantum Hall interferometers, Nat. Nanotechnol. **16**, 563 (2021).

[32] S.-C. Youn, H.-W. Lee, and H.-S. Sim, Nonequilibrium Dephasing in an Electronic Mach-Zehnder Interferometer, Phys. Rev. Lett. **100**, 196807 (2008).

[33] I. P. Levkivskyi and E. V. Sukhorukov, Dephasing in the electronic Mach-Zehnder interferometer at filling factor $\nu = 2$, Phys. Rev. B **78**, 045322 (2008).

[34] D. L. Kovrizhin and J. T. Chalker, Exactly solved model for an electronic Mach-Zehnder interferometer, Phys. Rev. B **80**, 161306(R) (2009).

[35] M. Schneider, D. A. Bagrets, and A. D. Mirlin, Theory of the nonequilibrium electronic Mach-Zehnder interferometer, Phys. Rev. B **84**, 075401 (2011).

[36] W. Liang, M. Bockrath, D. Bozovic, J. H. Hafner, M. Tinkham, and H. Park, Fabry-Perot interference in a nanotube electron waveguide, Nature (London) **411**, 665 (2001).

[37] N. Moreau, B. Brun, S. Somanchi, K. Watanabe, T. Taniguchi, C. Stampfer, and B. Hackens, Quantum Hall nano-interferometer in graphene, arXiv:2110.07979.

[38] N. Moreau, B. Brun, S. Somanchi, K. Watanabe, T. Taniguchi, C. Stampfer, and B. Hackens, Upstream modes and antidots poison graphene quantum Hall effect, Nat. Commun. **12**, 4265 (2021).

[39] C. de C. Chamon, D. E. Freed, S. A. Kivelson, S. L. Sondhi, and X. G. Wen, Two point-contact interferometer for quantum Hall systems, Phys. Rev. B **55**, 2331 (1997).